Chemical Science

ROYAL SOCIETY OF CHEMISTRY

EDGE ARTICLE

View Article Online
View Journal | View Issue

Cite this: *Chem. Sci.*, 2023, **14**, 11830

All publication charges for this article have been paid for by the Royal Society of Chemistry

Received 29th August 2023
Accepted 3rd October 2023

DOI: 10.1039/d3sc04532c

rsc.li/chemical-science

Ion sieving membrane for direct seawater anti-precipitation hydrogen evolution reaction electrode†

Qianfeng Liu, Zhao Yan, Jianxin Gao, Hefei Fan, Min Li and Erdong Wang *

In seawater, severe hydroxide-based precipitation on the hydrogen evolution reaction (HER) electrode surface is still a major stumbling block for direct seawater electrolysis. Here, we design a direct seawater HER electrode with excellent anti-precipitation performance based on an $Ni(OH)_2$ nanofiltration membrane *in situ* grown on nickel foam (NF) at room temperature. The positively charged $Ni(OH)_2$ membrane with nanometer-scale cracks realises an ion sieving function, which apparently hinders the transfer of Mg^{2+}/Ca^{2+} ions to suppress precipitation, while rapidly transporting OH^- and H_2O to ensure HER mass transfer. Therefore, the $Ni(OH)_2$-membrane-decorated seawater HER electrode reduces precipitation by about 98.3% and exhibits high activity and stability. Moreover, in the application of a direct seawater electrolyser and magnesium seawater battery, the $Ni(OH)_2$ membrane-decorated electrode also shows low precipitation and high stability. This work highlights a potential strategy to solve HER electrode precipitation in seawater *via* an ingenious electrode structure design.

Introduction

Hydrogen, a carbon-free fuel, can provide a practicable strategy to mitigate climate change and achieve carbon neutrality,[1–4] since it is generated through water electrolysis powered by clean energy, such as seawater electrolysis powered by off-shore wind power.[5–7] Compared with conventional alkaline and proton exchange membrane (PEM) water electrolysis, seawater electrolysis directly uses the seawater as a waterhead, which reduces the cost of hydrogen production by getting rid of the equipments to produce ultra-pure water.[8,9] However, impurity ions in seawater, *e.g.* Cl^- (20.06 g kg^{-1} H_2O) and Mg^{2+} (1.33 g kg^{-1} H_2O), are known to bring about challenges of the chlorine evolution reaction (ClER) on the oxygen evolution reaction (OER) electrode, equipment corrosion by Cl^-, and the precipitation of hydroxides on the hydrogen evolution reaction (HER) cathode.[10–13] Due to the effect of blanket cathode precipitation on the size of the active area, over 50% of the HER electrode current density is lost after only 24 hours of operation.[14,15] Moreover, HER electrode precipitation also causes problems for other applications, such as electrochemical sewage treatment, sodium hypochlorite production from seawater, and metal seawater batteries.[16–21] Therefore, an ideal method to solve HER electrode precipitation is urgently needed for applications.

The development of reported methods for solving HER electrode precipitation caused by Mg^{2+} and Ca^{2+} ions in seawater can be categorized into four types: (i) the addition of acid or inhibitor to the electrolyte, which avoids the formation of precipitate on the HER electrode, such as sulfuric acid to prevent precipitation and CO_2 to dissolve $CaCO_3$;[22–25] (ii) optimizing the operating conditions or electrolyser structure, such as current density, electrolyte flow rate, and ion exchange membrane, that can scour the precipitate on the electrode by hydrogen gas bubbles and electrolyte, or an Na^+ exchange membrane to alleviate the formation of Mg^{2+} and Ca^{2+} precipitates;[26–28] (iii) washing with acid, that can dissolve the alkaline precipitate;[15] and (iv) direct pre-removal of Mg^{2+} and Ca^{2+} ions, which eliminates the main precipitate-forming ions, as used in the chlor-alkali industry for example.[29] Some of these methods can efficiently prevent the formation of precipitate, but incidental problems make large-scale application for seawater electrolysis difficult, such as acid consumption and corrosion because of acid addition or wash, and the high cost of the pre-removal of the ions. If the HER electrode surface could itself prevent the formation of precipitate, such as a Cr_2O_3 Lewis acid layer, which hinders the transfer of the OH^- produced by the HER electrode to lower the electrode surface pH,[30] this would be more significant for real applications. Several groups have revealed this phenomenon and the reason for the precipitation adsorption on the HER electrode, but studies of how to obtain an anti-precipitation HER electrode in seawater are limited.[31]

Herein, an $Ni(OH)_2$ ion sieving membrane coated on the surface of 3D NF was *in situ* fabricated as an anti-precipitation

Dalian National Laboratory for Clean Energy, Dalian Institute of Chemical Physics, Chinese Academy of Sciences, Dalian 116023, China. E-mail: edwang@dicp.ac.cn

† Electronic supplementary information (ESI) available. See DOI: https://doi.org/10.1039/d3sc04532c

HER electrode in seawater. Combined theoretical calculation and experimental tests, the $Ni(OH)_2$ ion sieving membrane can efficiently hinder the transfer of Mg^{2+}/Ca^{2+} ions and rapidly convey the HER related OH^- and H_2O due to the positive charge and nanometer-scale cracks. Due to the excellent anti-precipitation performance, rapid mass transfer, and synergistic effect between $Ni(OH)_2$ and NF, the $Ni(OH)_2$–NF electrode can reduce most of the precipitation on the surface, and exhibit higher HER performance than that of an NF electrode. In application to a direct seawater electrolyser and magnesium seawater battery, the $Ni(OH)_2$-membrane-coated electrode also obviously adsorbed less precipitation and displayed higher stability.

Results and discussion

Precipitation on a seawater HER electrode

To understand which ion in seawater led to the precipitation, the seawater-related Mg^{2+}, Ca^{2+}, SO_4^{2-} and HCO_3^- ions were separated. As shown in Fig. 1a, the NF-based HER electrodes were measured in 3.5% NaCl without or with the different ions at the same concentration in seawater under 1 mA cm^{-2} for 200 h. Distinctly, the precipitation was mainly caused by the Mg^{2+} ion and partly by the Ca^{2+} ion, because the precipitation mass on the electrode surface suddenly increased from 1.4–9.0 mg cm^{-2} to 215–229 mg cm^{-2} when the electrolytes contained Mg^{2+} ions, and the HER electrodes were fully covered by a burly white precipitate. The main components of the precipitate on the electrode surface were $Mg(OH)_2$ and adsorbed NaCl, as identified by XRD (Fig. 1b). It is speculated that the pH on the seawater HER electrode surface would increase rapidly at the beginning of HER operation, as schematically illustrated in Fig. 1c, which was much higher than the pH of $Mg(OH)_2$ deposition.[32,33] Therefore, the Mg^{2+} ions in seawater would preferentially deposit on the surface of the HER electrode, and then the $Mg(OH)_2$ precipitate on the electrode would act as deposition sites for the newly formed $Mg(OH)_2$.[26] As a result, the seawater HER electrode would be covered with $Mg(OH)_2$-based precipitate.

Synthesis and characterization of the $Ni(OH)_2$ membrane

To solve the precipitation on a direct seawater HER electrode, an $Ni(OH)_2$ membrane was *in situ* synthesized on NF (1 cm × 2

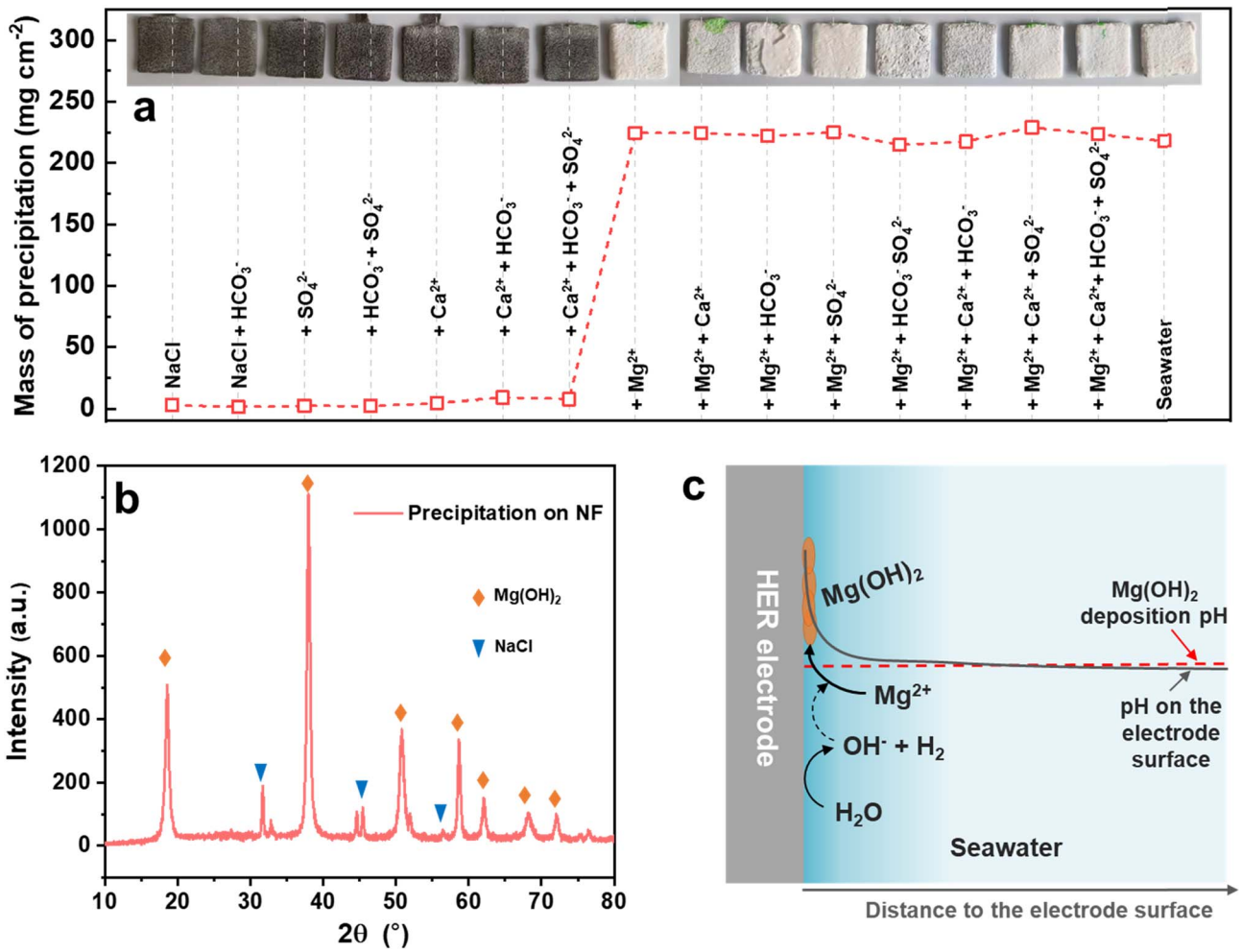

Fig. 1 (a) Mass of precipitation on the electrode in different electrolytes (inset: photographs of the HER electrode after measurement). (b) XRD pattern of the precipitation. (c) A schematic illustration of the precipitation mechanism on the HER electrode surface in seawater.

cm) *via* a simple soaking process in 0.1 M $NiCl_2$ for 3 days at 25 ± 1 °C, as schematically illustrated in Fig. 2a. During the soaking period, the NF was etched by the dissolved oxygen and Cl^-, and then the generated OH^- reacted with the excess Ni^{2+} to generate a positively charged $Ni(OH)_2$ membrane ($\zeta = +23.8$ mV in 1 mM NaOH, Fig. 2b) on the NF surface. Due to the positive charge, the $Ni(OH)_2$ membrane can hinder the passage of Mg^{2+} and Ca^{2+} ions through the membrane from the electrolyte to the NF surface, as will be discussed in detail below.

As disclosed in Fig. 2c, the diffraction peaks appearing at 19.3°, 33.1°, 38.5°, and 52.1° were assigned to the characteristic (001), (100), (101) and (102) facets for $Ni(OH)_2$ (JCPDS no. 74-2075), respectively. It is noteworthy that the *c*-axis-related diffraction peaks were broadened due to the disordered and expanded $Ni(OH)_2$ layers. The higher redox peak current of Ni(II) to Ni(III) for the $Ni(OH)_2$–NF electrode compared to the NF electrode further verified that the NF surface was covered with $Ni(OH)_2$ (Fig. S1†). The morphology of the $Ni(OH)_2$ membrane on NF was studied with field emission scanning electron microscopy (SEM). As shown in Fig. 2d, $Ni(OH)_2$ was uniformly coated around the 3D NF surface to form the membrane. The surface of the $Ni(OH)_2$ membrane was formed by continuous scarf-like $Ni(OH)_2$ sheets with rugged pores (Fig. 2e). In the membrane matrix, with a thickness of ~520 nm (Fig. 2f), the

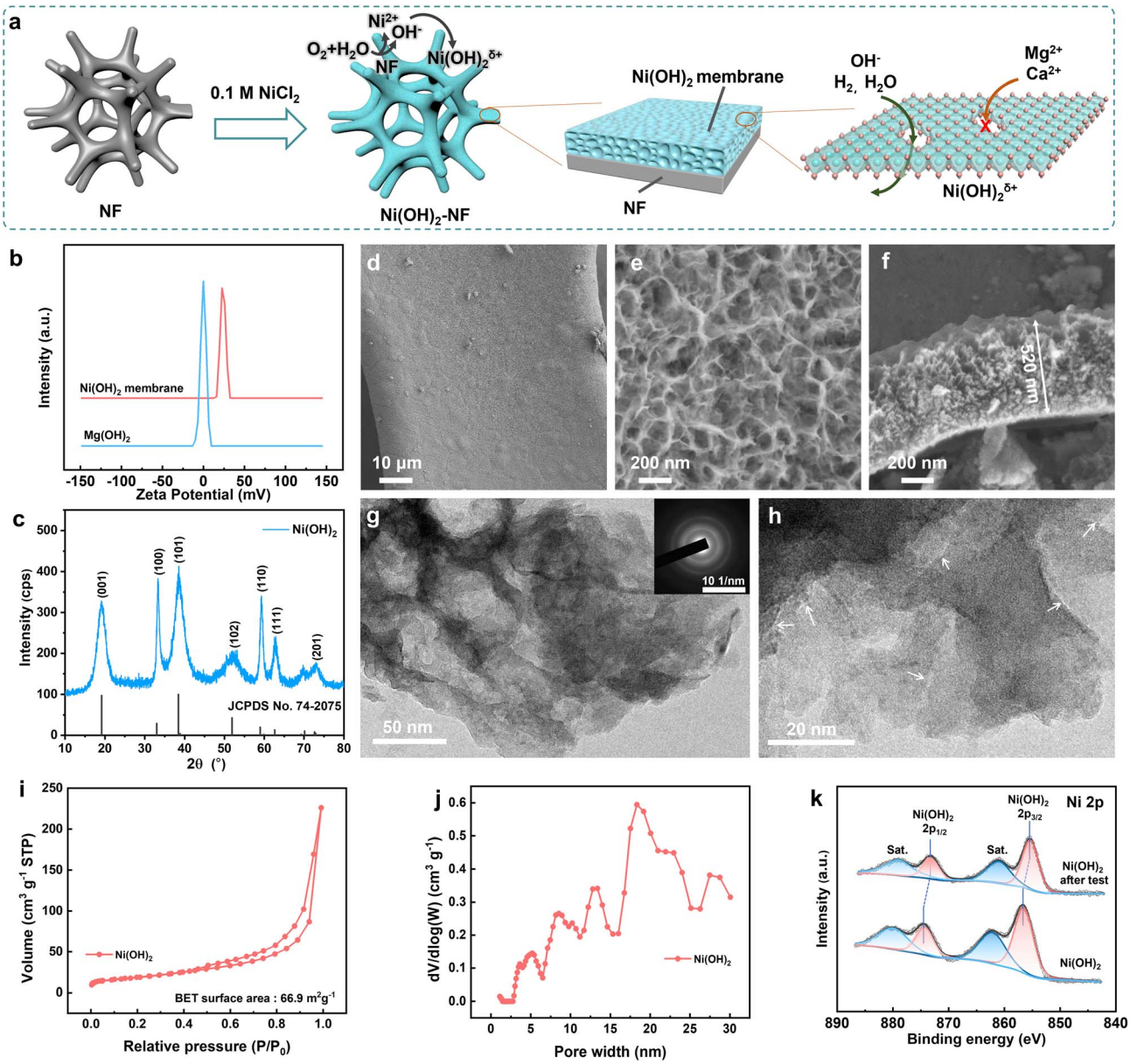

Fig. 2 (a) Schematic illustration of *in situ* growth of the $Ni(OH)_2$ membrane on NF. (b) Zeta potential of the $Ni(OH)_2$ membrane stripped from $Ni(OH)_2$–NF electrodes and precipitated $Mg(OH)_2$. (c) XRD pattern of the $Ni(OH)_2$ membrane. (d–f) Typical SEM, and (g, h) TEM images of the $Ni(OH)_2$ membrane (inset: SADE). (i) N_2 isothermal absorption/desorption and (j) pore size distribution curves of the $Ni(OH)_2$ membrane stripped from the $Ni(OH)_2$–NF electrodes. (k) High-resolution XPS spectra for Ni 2p of the $Ni(OH)_2$ membrane before and after testing in seawater.

rugged pores were completely filled with amorphous $Ni(OH)_2$. Therefore, the solutions must pass through the amorphous $Ni(OH)_2$ sheets to cross over the membrane, but not through the pores. To obtain detailed structural information about the $Ni(OH)_2$ membrane, a transmission electron microscopy (TEM) investigation was carried out. The TEM and selected area electron diffraction (SADE) results further verified the porous and amorphous structure of the $Ni(OH)_2$ membrane (Fig. 2g). Under higher magnification (Fig. 2h), the crack-like defects were randomly distributed on the $Ni(OH)_2$ sheets with a width of 0.4–2.0 nm and a length of 7.9–26.2 nm. The defects supply enough high-speed channels for the water and ions to cross over the $Ni(OH)_2$ membrane, which will be discussed in detail *via* the simulation below.

Brunauer–Emmett–Teller (BET) analysis showed that the $Ni(OH)_2$ membrane possessed a specific area of 66.9 $m^2\ g^{-1}$ (Fig. 2i); the pore size was distributed over 2.5 nm and centred around 20 nm (Fig. 2j), which was in agreement with the TEM results. The surface chemical state of the $Ni(OH)_2$ membrane was investigated with X-ray photoelectron spectroscopy (XPS). As revealed in Fig. S2,† the $Ni(OH)_2$ membrane contained only Ni, O, and C elements. For the Ni 2p XPS spectra (Fig. 2k), the two spin–orbit doublet peaks at 856.4 and 874.3 eV with two shake-up satellites at 862.0 and 880.0 eV belong to $Ni(OH)_2$. The absence of an Ni(0) binding energy peak in Fig. 2k further confirmed that the surface of NF was fully coated with the $Ni(OH)_2$ membrane. The species of $Ni(OH)_2$ was also demonstrated by the O 1s XPS spectra at a binding energy of 531.7 eV (Fig. S3†). Moreover, impurities of H_2O and CO_3^{2-} were found in the $Ni(OH)_2$ membrane in the O 1s XPS spectra (the CO_3^{2-} can also be confirmed by the C 1s XPS spectra, Fig. S4†). The impurity mass was calculated to be about 5.8% from the thermal gravimetric analysis (TGA, Fig. S5†) curves. In short, the positively-charged $Ni(OH)_2$ membrane with nanometer-scale cracks was *in situ* uniformly coated on the 3D NF.

Anti-precipitation performance

Firstly, we studied the precipitation mass influenced by the thickness of the $Ni(OH)_2$ membrane on the NF electrode, which was controlled by soaking time. From 1 to 5 days (Fig. S6†), the thickness of the $Ni(OH)_2$ membrane grew from ~350 nm to ~1010 nm, as detected by SEM. During the measurement, we found that the Ni flake, Ti mesh and graphite rod as counter electrode (CE) in seawater all suffered from corrosion and a chlorine evolution reaction. To avoid or reduce the effect of the CE on the working electrode (WE) as much as possible, we chose a pure Mg rod as the counter electrode. During the test, the Mg CE would be oxidized into Mg^{2+}. When the WE was separated from the CE by AEM, the generated Mg^{2+} would not affect the WE. Without the AEM, the Mg^{2+} would diffuse to the WE cell to supplement the consumed Mg^{2+}. Compared to an NF electrode, the $Ni(OH)_2$–NF electrodes deposited less precipitation after 12 h of measurement at 10 mA cm^{-2} in seawater when the WE and CE were separated with AEM (marked as SW + AEM, Fig. 3a, S7 and S8†). Due to the lower precipitation, the $Ni(OH)_2$–NF electrodes exhibited higher stability than the NF electrode (Fig. S9†). With increasing soaking time, the precipitation mass reached a minimum value of 3.2 mg cm^{-2} for the $Ni(OH)_2$–NF-3d electrode. In detail, the porous precipitation of Mg/Ca-based hydroxide or carbonate with a thickness of 6.1 μm was evenly distributed on the surface of the $Ni(OH)_2$ membrane (Fig. S2, S10–S12†). It is worth noting that the Mg and Ca elements were only distributed on the surface of the $Ni(OH)_2$ membrane (Fig. S11†), indicating that the $Ni(OH)_2$ membrane can hinder the transfer of Mg^{2+} and Ca^{2+} from seawater to the NF substrate. Moreover, the $Ni(OH)_2$–NF electrodes displayed higher HER performance than NF because of the synergistic effect between $Ni(OH)_2$ and NF to accelerate the Volmer step of HER.[34,35] Therefore, the potential of $Ni(OH)_2$–NF electrodes (−1.078 to −1.067 V *vs.* SCE, saturated calomel electrode) was more positive with 24 to 35 mV than that of the NF electrode (−1.102 V *vs.* SCE) at a current density of 10 mA cm^{-2} (Fig. 3b). The smaller Tafel slopes and R_{CT} in EIS of the $Ni(OH)_2$–NF electrodes also confirmed the higher HER activity for $Ni(OH)_2$–NF electrodes (Fig. S13†). Just to be clear, the electrolyte pH kept rising from ~8.1 to 12.8 during the measurement, so the SCE was better able to act as the reference electrode but not as a reversible hydrogen electrode (RHE).

To further reduce the precipitation on the electrode surface, we then added $Mg(OH)_2$ powder in seawater to obtain a saturated $Mg(OH)_2$ seawater solution, denoted SW + $Mg(OH)_2$. The $Mg(OH)_2$ particles were expected to supply nucleation sites in seawater electrolyte for the newly formed $Mg(OH)_2$, resulting in new $Mg(OH)_2$ precipitate being deposited in the electrolyte but not on the HER electrode surface. As shown in Fig. 3c and S14,† the precipitation on the $Ni(OH)_2$–NF electrode in SW + AEM (3.2 mg cm^{-2}) obviously decreased after the addition of $Mg(OH)_2$ in seawater (SW + $Mg(OH)_2$ + AEM, 0.4 mg cm^{-2}), but the effect on the NF electrode was insignificant. Additionally, the electrolytic cell without AEM was also investigated, in which case the working electrode chamber would be sustainingly supplied with Mg^{2+} ions from the counter electrode during the measurement. As a result, in seawater, the precipitation mass for the $Ni(OH)_2$–NF electrode increased significantly from 3.2 to 38.5 mg cm^{-2}, but only increased slightly from 0.4 to 0.9 mg cm^{-2} in SW + $Mg(OH)_2$ (Fig. 3c). It was demonstrated that the $Ni(OH)_2$ membrane assisted by saturated $Mg(OH)_2$ in seawater can dramatically reduce the precipitation on the HER surface, and the reduction in mass percentage reached 98.3%. Therefore, the lower precipitation on the electrode brought about higher stability for the $Ni(OH)_2$–NF electrode (Fig. S15†).

We then evaluated the stability of the $Ni(OH)_2$ membrane by prolonging the test time. As demonstrated in Fig. 3d and S16,† the NF and $Ni(OH)_2$–NF electrodes were measured under SW + $Mg(OH)_2$ + AEM conditions every 20 h to obtain the precipitation mass over a total time of 100 h. The precipitation mass of the $Ni(OH)_2$–NF electrode was much lower than that of NF over the whole test time. At the time of 100 h, the precipitation mass of the $Ni(OH)_2$–NF electrode was 5.3 mg cm^{-2}, which was only 10.9% that of the NF electrode (48.5 mg cm^{-2}). Due to the accumulation of precipitation, the NF electrode exhibited poor stability with an increased overpotential of 56 mV compared to

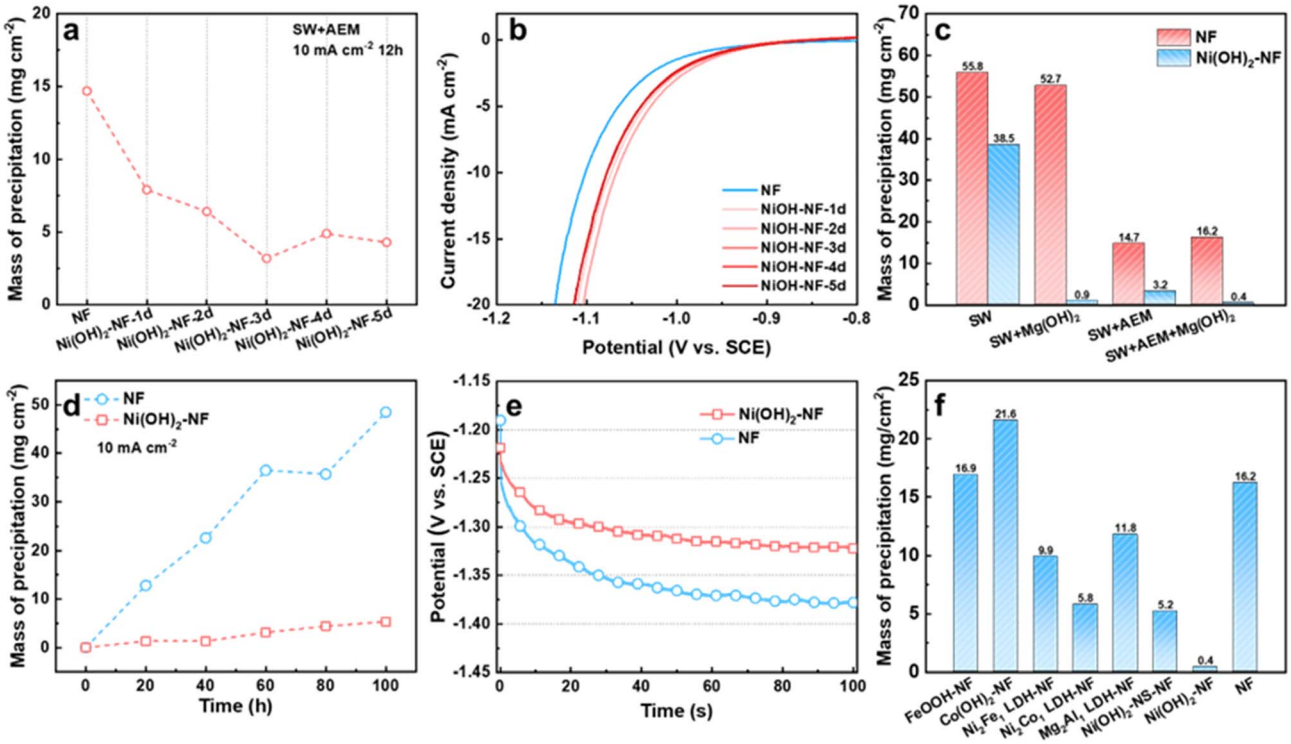

Fig. 3 (a) Mass of precipitation on the electrodes, and (b) the LSV curves of the electrodes under different deposition times. Mass of precipitation on the NF and $Ni(OH)_2$–NF electrodes, (c) under different conditions, and (d) with different measure times. (e) Chronopotentiometry curves of NF and $Ni(OH)_2$–NF electrodes with the electrolyte replaced every 20 h under a current density of 10 mA cm^{-2}. (f) Mass of precipitation on the different kinds of hydroxide-decorated electrodes.

the $Ni(OH)_2$–NF electrode at the measurement time of 100 h for the continuous test (Fig. 3e).

Finally, we also tried to obtain other hydroxide membranes decorated on NF with the same fabrication conditions as the $Ni(OH)_2$ membrane, such as FeOOH–NF, $Co(OH)_2$–NF, Ni_2Fe_1 LDH–NF, Ni_2Co_1 LDH–NF, and Mg_2Al_1 LDH–NF electrodes. For these electrodes, only the Ni_2Co_1 LDH/NF electrode formed an $Ni(OH)_2$-membrane-like structure (Fig. S17†), which exhibited higher anti-precipitation performance than the other electrodes, but much lower than that of the $Ni(OH)_2$–NF electrode under SW + $Mg(OH)_2$ + AEM conditions (Fig. 3f, S18†). When the $Ni(OH)_2$ membrane was changed to nanosheets, such as an $Ni(OH)_2$-NS-NF electrode, it displayed similar anti-precipitation performance to the Ni_2Co_1 LDH–NF electrode. This indicated that the excellent anti-precipitation performance of the $Ni(OH)_2$–NF electrode arose from the special structure of the $Ni(OH)_2$ membrane. Moreover, these hydroxide membranes would reduce the HER performance of NF, or display lower HER performance than that of the $Ni(OH)_2$–NF electrode (Fig. S19†).

Anti-precipitation mechanism

As described above, the $Ni(OH)_2$ membrane reduces the precipitation by hindering the transfer of Mg^{2+} from the electrolyte to the electrode surface. To understand the mechanism, we quantified the transfer rate of Mg^{2+} and compared it with the other ions. For the $Ni(OH)_2$ membrane on NF it was difficult to obtain the mass transfer rate of Mg^{2+}, so we fabricated numerous $Ni(OH)_2$–NF electrodes and treated them with ultrasound to obtain an $Ni(OH)_2$ membrane turbid liquid. *Via* a vacuum filtration method,[36] an $Ni(OH)_2$ membrane with a thickness of 1.4 μm on a nylon filter membrane was prepared (Fig. S20†).

The $Ni(OH)_2$ membrane was then sealed with a 2 cm^2 opening in copper tape, and clamped in the test setup (Fig. 4a and S21†). Prior to the conductivity test, the relationship between conductivity (σ) and concentration (c) was determined for NaOH, NaCl, KCl, $CaCl_2$, $MgCl_2$, $NaNO_3$, Na_2CO_3, and Na_2SO_4 solutions, which was $\log(\sigma) = a + \log(c)$ (Fig. S22†). Then the conductivity change with time was measured for different concentrations of NaOH and $MgCl_2$ solutions (Fig. S23†). Finally, the ion permeation rate through the nylon membrane (substrate) and the $Ni(OH)_2$-membrane-coated substrate was obtained. As shown in Fig. 4b, the ion permeation rate of the NaOH solution increased linearly with concentration for both substrate and $Ni(OH)_2$-membrane-coated substrate, and the slopes for these two lines were very close. This suggested that the NaOH passed through the $Ni(OH)_2$ membrane almost without resistance, as the ion difference values of the permeation rates between the $Ni(OH)_2$-membrane-coated substrate and the substrate were the ion hindrance rates in the $Ni(OH)_2$ membrane. However, for $MgCl_2$ solution (Fig. 4c), the linear slope of the $Ni(OH)_2$-membrane-coated substrate was much lower than that of the substrate, indicating the obvious resistance for $MgCl_2$ to pass through the $Ni(OH)_2$ membrane. The

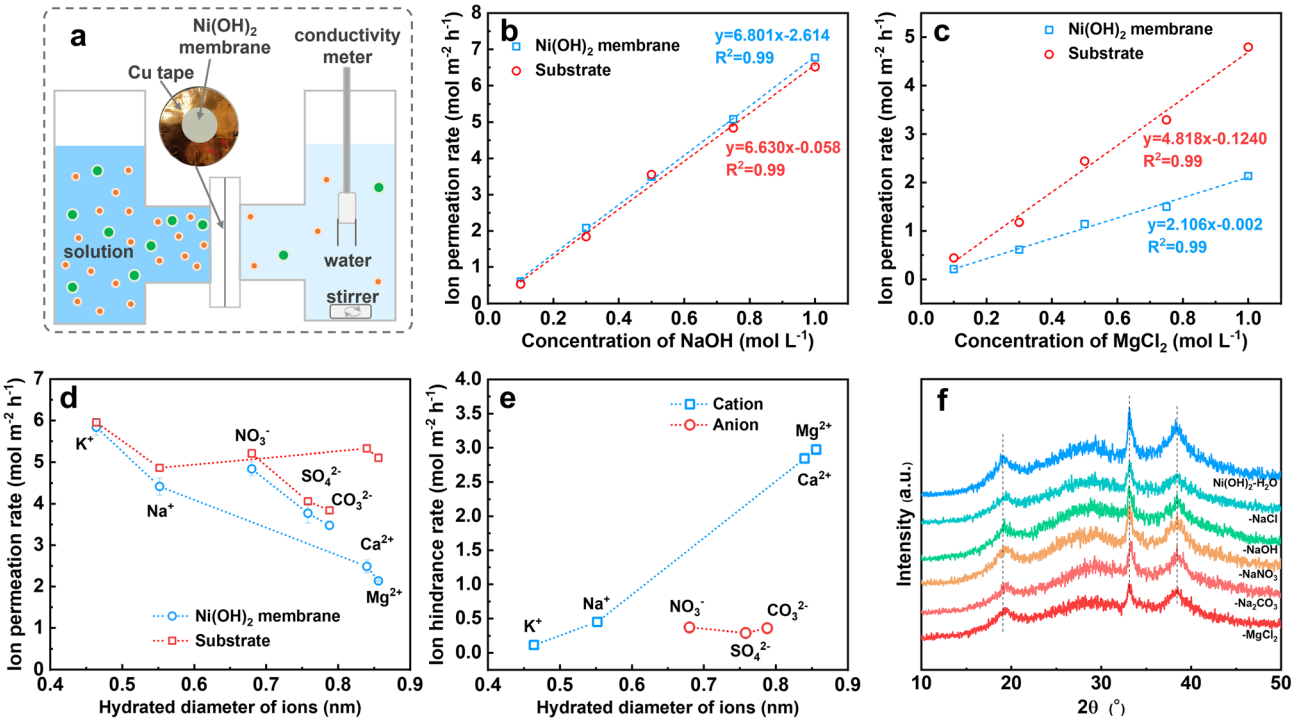

Fig. 4 (a) Schematic of $Ni(OH)_2$ membrane test setup. Ion permeation rates under different concentrations of (b) NaOH and (c) $MgCl_2$ solutions. (d) Ion permeation rate *versus* ion hydrated diameter of the substrate and $Ni(OH)_2$-membrane-coated substrate. (e) The calculated ion hindrance rate for the $Ni(OH)_2$ membrane. (f) XRD patterns of $Ni(OH)_2$ membrane powder after immersion in different solutions.

other solutions were measured at a concentration of 1 M using the same method (Fig. S24†), and the ion permeation rates for the K^+, Na^+, Ca^{2+}, Mg^{2+}, NO_3^-, SO_4^{2-} and CO_3^{2-} passing through the substrate and $Ni(OH)_2$-membrane-coated substrate were calculated. As listed in Fig. 4d, the cation permeation rates decreased with increasing hydrated diameter when passing through the $Ni(OH)_2$-membrane-coated substrate, but with slight change through the substrate. For anions, the permeation rates decreased with the increasing hydrated diameter both in the substrate and in the $Ni(OH)_2$-membrane-coated substrate. The difference in values of the ion permeation rates between the $Ni(OH)_2$ membrane-coated substrate and the substrate is the ion hindrance rate, which represents the ion transfer rate in the $Ni(OH)_2$ membrane. As displayed in Fig. 4e, the ion hindrance rates of Mg^{2+} and Ca^{2+} (2.97 and 2.84 mol m^{-2} h^{-1}) were much higher than those of Na^+ and K^+ (0.45 and 0.12 mol m^{-2} h^{-1}), which increased with the hydrated ion diameter. However, NO_3^-, SO_4^{2-} and CO_3^{2-} exhibited similar hindrance rates (0.29–0.37 mol m^{-2} h^{-1}), which were close to that of Na^+. The ion hindrance feature of the $Ni(OH)_2$ membrane, strong resistance for high-valence ions (Mg^{2+} and Ca^{2+}) but weak resistance for low-valence ions (K^+ and Na^+) and reverse ions (NO_3^-, SO_4^{2-} and CO_3^{2-}), is consistent with the nanofiltration membrane.

The interlayer distance of the $Ni(OH)_2$ nanosheets was about 0.46 nm as calculated with the Bragg equation, even though the atom size was ignored, which was smaller than the hydrated diameters of the ions as described before, especially for the anions of NO_3^-, SO_4^{2-} and CO_3^{2-}. The narrow interlayer distance would result in strong resistance to the transfer of the anions. If the interlayering of $Ni(OH)_2$ nanosheets could transfer the ions rapidly, the interlayer distance should be expanded by ions such as GO or α-$Ni(OH)_2$, which could be obviously detected by XRD.[37–39] However, as shown in Fig. 4f, the position and width of the XRD diffraction peaks of the $Ni(OH)_2$ membrane were unchanged even though the $Ni(OH)_2$ membrane had been immersed in H_2O solution with 1 M of NaCl, NaOH, $NaNO_3$, Na_2CO_3 and $MgCl_2$ for over one month. This suggested that no or only a very small amount of water or ions could be inserted in the layer space for the $Ni(OH)_2$ sheets. Therefore, it is very difficult for the ions to pass through the $Ni(OH)_2$ membrane *via* the interlayer of $Ni(OH)_2$ sheets, which is in accord with reports.[40–43] For the nanometer-scale cracks in Fig. 2i, the size of cracks with a width of 0.4–2.0 nm was larger than the hydrated diameters of the ions, which ensured high permeation for all the tested ions.[44] However, the high-value cations of Mg^{2+} and Ca^{2+} encountered obviously higher resistance than anions with a similar hydrated diameter, which might be hindered by electrostatic repulsion due to the positively charged $Ni(OH)_2$ membrane.

In light of the molecular dynamics simulation, we investigated the ion transfer rate as the ions passed through the $Ni(OH)_2$ membrane and were affected by the positive charge. The optimized model of a monolayer $Ni(OH)_2$ sheet with an opening of 3 × 5 Ni atoms is displayed in Fig. 5a. To simulate the transfer rate of Mg^{2+}, Na^+, Cl^-, OH^- and H_2O, and to avoid the deposition interference between Mg^{2+} and OH^-, the simulation was divided into $MgCl_2$ and NaOH solution systems, as shown in Fig. 5b and c. The $MgCl_2$ and NaOH solution was up to

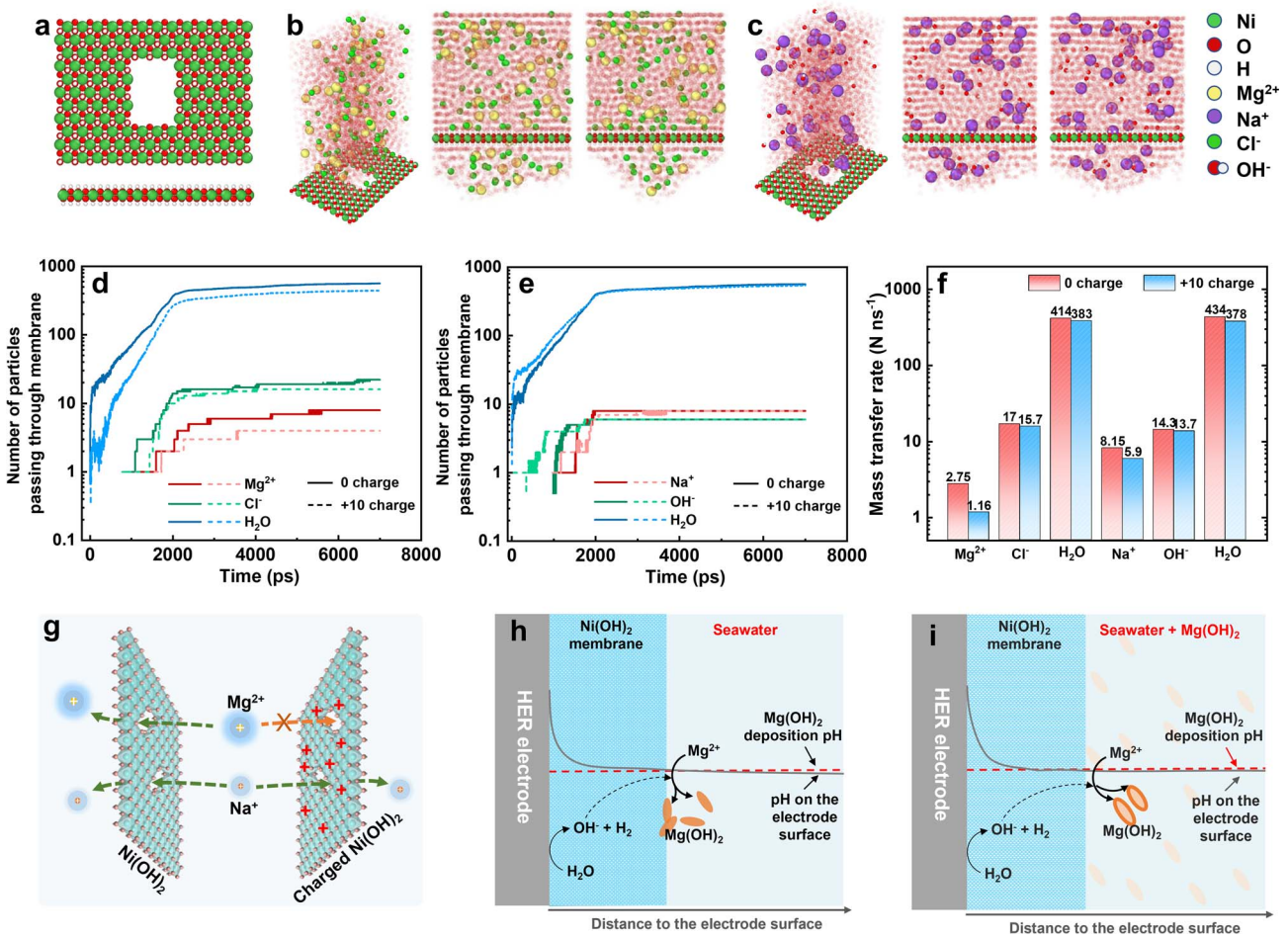

Fig. 5 Simulations of ion sieving for the $Ni(OH)_2$ membrane. (a) The optimized opening monolayer $Ni(OH)_2$ nanosheet structure in top and side view. Initial and final simulation snapshots of the (b) $MgCl_2$ and (c) NaOH solutions. The number of (d) Mg^{2+}, Cl^-, and H_2O, (e) Na^+, OH^-, H_2O, and (f) mass transfer rates of the simulated particles passing through the charged and uncharged $Ni(OH)_2$ nanosheet. (g) Ion sieving mechanism for the $Ni(OH)_2$ nanosheets with and without positive charge. Schematic illustration of (h) the precipitation mechanism on the HER electrode without an $Ni(OH)_2$ membrane in seawater, and (i) anti-precipitation mechanism for the $Ni(OH)_2$-membrane-decorated HER electrode in seawater with saturated $Mg(OH)_2$.

the $Ni(OH)_2$ sheet at 300 K and 1 atm and bounded with a simulation box. At the top of the $MgCl_2$ and NaOH solution, a transparent wall with 1 atm pressure drove the solution to pass through the opening on the $Ni(OH)_2$ sheet (Fig. S25 and S26†). The number of ions and water molecules that passed was counted by the LAMMPS software package and recorded in Fig. 5d and e, including the 0-charged and +10-charged $Ni(OH)_2$ models. Apart from Mg^{2+}, the number of other ions and water molecules passing through the $Ni(OH)_2$ sheet with or without positive charge was unchanged or changed insignificantly. According to the slope, the number of ions or water molecules passing through the $Ni(OH)_2$ sheet with increasing time, the mass transfer rate was calculated as shown in Fig. 5f. When the $Ni(OH)_2$ sheet was positively charged, the mass transfer rate of Mg^{2+} dropped by 57.8% from 2.75 to 1.16 no. ns^{-1}, while Na^+ dropped by only 27.6% from 8.15 to 5.90 no. ns^{-1}. The anions of Cl^- and OH^- and the water molecules were almost unchanged. This suggested that the positive charge on the $Ni(OH)_2$ sheet obviously changed the ion sieving behaviour, hindering high-valence cations with much stronger resistance than those of low-valence cations, anions and molecules.

Therefore, the positively charged $Ni(OH)_2$ membrane can sieve out Mg^{2+} with higher efficiency. For the $Ni(OH)_2$ membrane without charge, Mg^{2+} and Na^+ can rapidly pass through the $Ni(OH)_2$ nanosheet *via* the crack-like defects, but not through the interlayer between $Ni(OH)_2$ layers (left-hand side of Fig. 5g). But for the $Ni(OH)_2$ membrane with positive charge, the electrostatic repulsive force between Mg^{2+} ions and the $Ni(OH)_2$ nanosheet would lower the transfer rate of Mg^{2+} ions, and evidently reduce the mass transfer rate of Mg^{2+} ions passing through the $Ni(OH)_2$ membrane (right-hand side of Fig. 5g). This should illustrate that the higher mass transfer rate of water and Cl^- was beneficial to passing a greater number of these than of Mg^{2+}, Na^+ or OH^-. Therefore, normalizing the mass transfer rates to the number (percentage transfer rate) makes the comparison easier. As listed in Table S1,† the rank of ion transfer rate was $OH^- > Cl^- > Na^+ > Mg^{2+}$, which is associated with the ionic diffusion coefficient.[45]

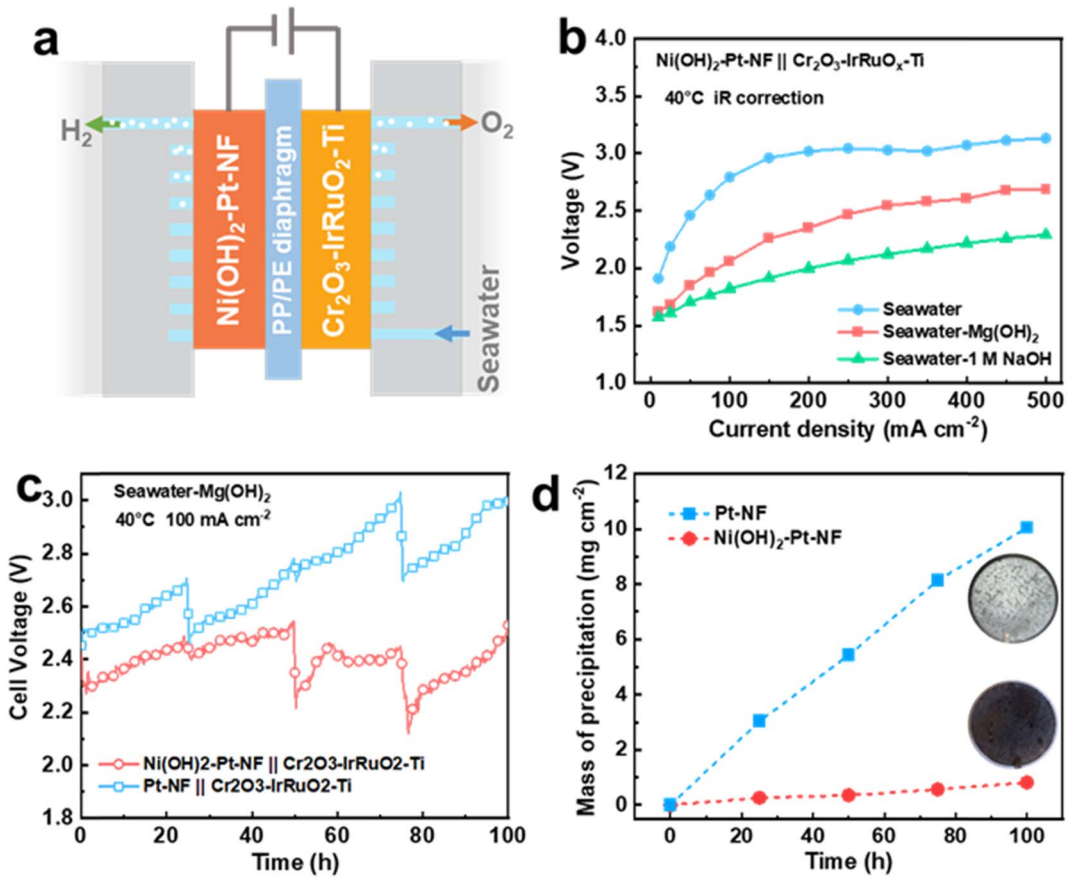

Fig. 6 (a) A schematic illustration of a direct seawater electrolyser equipped with an $Ni(OH)_2$–Pt–NF electrode. (b) The polarization curves of an $Ni(OH)_2$–Pt–NF-electrode-equipped electrolyser in different electrolytes. (c) Galvanostatic discharge curves of electrolysers at a current density of 100 mA cm^{-2} and (d) mass of precipitation on the $Ni(OH)_2$–Pt–NF and Pt–NF electrodes (inset: photographs of the HER electrodes after 100 h of measurement).

Combining the anti-precipitation performance and ion transfer behaviour of the $Ni(OH)_2$ membrane, the anti-precipitation mechanism of the $Ni(OH)_2$–NF electrode is illustrated below. For the HER electrode with an $Ni(OH)_2$ membrane in seawater (Fig. 5h), the pH on the surface would increase dramatically at the begin of HER process, but the Mg^{2+} could not pass through the $Ni(OH)_2$ membrane to form the precipitate. With increasing time, the out-diffusion of OH^- would raise the pH on the interface between the $Ni(OH)_2$ membrane and seawater to reach the deposition pH, so the formed $Mg(OH)_2$ would be deposited both on the $Ni(OH)_2$ membrane and in seawater. Hence, in seawater, the $Ni(OH)_2$ membrane could reduce the electrode precipitation, but the effect was slight.

When the seawater had saturated $Mg(OH)_2$ added (Fig. 5i), the pH on the $Ni(OH)_2$ membrane surface would reach the $Mg(OH)_2$ deposition pH at the initial operation time. After operation, the seawater pH near the $Ni(OH)_2$ membrane surface would soon be slightly higher than the $Mg(OH)_2$ deposition pH to deposit Mg^{2+}. Meanwhile, the saturated $Mg(OH)_2$ particles in the seawater supplied abundant nucleation sites for the newly formed $Mg(OH)_2$. Therefore, most of the $Mg(OH)_2$ was deposited in the saturated $Mg(OH)_2$ seawater, and only a little $Mg(OH)_2$ was adsorbed on the $Ni(OH)_2$ membrane surface. This is the mechanism whereby the $Ni(OH)_2$–NF electrode exhibits excellent anti-precipitation performance in saturated $Mg(OH)_2$ seawater. If the HER electrode without an $Ni(OH)_2$ membrane was operated directly in saturated $Mg(OH)_2$ seawater (Fig. S27†), the much higher pH on the electrode surface would also make it a faster nucleation site than that in seawater, which could not decrease the precipitation on the electrode surface.

Anti-precipitation membrane application

To broaden the application scope of the $Ni(OH)_2$ membrane and enhance its seawater HER performance, we chose Pt-based $Ni(OH)_2$–Pt–NF and Pt–NF electrodes to replace the $Ni(OH)_2$–NF and NF electrodes. As displayed in Fig. S28,† the Pt nanoparticles were uniformly dispersed on the surface of NF for the Pt–NF electrode, and the covered $Ni(OH)_2$ membrane exhibited similar structure and thickness to those of the $Ni(OH)_2$–NF electrode. Due to the high activity of Pt, the Pt–NF and $Ni(OH)_2$–Pt–NF electrodes as expected displayed obviously higher performance than that of the NF electrode (Fig. S29†). To further verify the anti-precipitation performance of the membrane-decorated electrode in application, we assembled a flow-type direct seawater electrolyser equipped with an

$Ni(OH)_2$–Pt–NF HER electrode and Cr_2O_3–$IrRuO_2$–Ti OER electrode (Fig. 6a) with a working area of 10 cm^2. Moreover, to lessen the trapped bulky $Mg(OH)_2$ particles in the NF pores of the HER electrode, we chose a PP/PE porous membrane as a diaphragm, and the electrolyte was fed only into the anode side to filter the bulky particles. Due to the higher pH of SW + $Mg(OH)_2$, the electrolyser in SW + $Mg(OH)_2$ exhibited much higher performance than that in seawater (Fig. 6b). The cell voltage (with 75% *iR* compensation) at 40 °C of the electrolyser in SW + $Mg(OH)_2$ was only 2.69 V at a current density of 500 mA cm^{-2}, while it was over 3.1 V in seawater and 2.29 V in seawater with 1 M NaOH. For the 100 h stability test at a current density of 100 mA cm^{-2}, the seawater electrolyser equipped with $Ni(OH)_2$–Pt–NF and Pt–NF electrodes had a similar cell voltage close to 2.4 V at the beginning (Fig. 6c). With increasing time, the seawater electrolyser voltage of the Pt–NF electrode increased faster than that of the $Ni(OH)_2$–Pt–NF electrode. For example, at a time of 100 h, the voltage reached 2.97 V for the Pt–NF-electrode-equipped seawater electrolyser, but it was only 2.48 V for the $Ni(OH)_2$–Pt–NF electrode. That means the $Ni(OH)_2$–Pt–NF electrode is much more stable than the Pt–NF electrode in seawater. Combined with the result in Fig. 3, the higher voltage of the Pt–NF-electrode-equipped seawater electrolyser was mainly caused by the greater precipitation on the electrode (Fig. 6d and S30†). At 100 h, the precipitation mass on the $Ni(OH)_2$–Pt–NF electrode was 0.82 mg cm^{-2}, which was only 8.1% that of the Pt–NF electrode (10.06 mg cm^{-2}). Besides, the $Ni(OH)_2$–Pt–NF electrode also exhibited higher anti-precipitation performance and stability than the Pt–NF electrode in a magnesium seawater battery (Fig. S31†). The results once again confirmed that an $Ni(OH)_2$ membrane on the electrode can obviously decrease the electrode surface precipitation to enhance its stability.

Conclusions

In summary, an $Ni(OH)_2$ nanofiltration membrane *in situ* grown on a 3D NF-based electrode was fabricated at room temperature *via* a simple chemical soaking method. Simulations and experiments revealed that the positively charged $Ni(OH)_2$ membrane with nanometer-scale cracks evidently hindered the transfer of Mg^{2+} and Ca^{2+}, while rapidly transferring OH^- and H_2O. In seawater, the $Ni(OH)_2$-membrane-decorated $Ni(OH)_2$–NF HER cathode reduced the Mg^{2+}-ion-induced precipitation on the electrode surface compared to the NF cathode. Due to the abundant nucleation sites from the added saturated $Mg(OH)_2$ in seawater at the initial operation, the $Ni(OH)_2$–NF cathode further dramatically reduced the precipitation by about 98.3%. Moreover, the $Ni(OH)_2$–NF electrode exhibited slightly higher HER activity and stability than the NF electrode due to the rapid transfer of OH^- and H_2O, the synergistic effect between $Ni(OH)_2$ and the Ni substrate, and the excellent anti-precipitation performance. In the application of a direct seawater electrolyser and MSWB, the $Ni(OH)_2$–Pt–NF electrode also displayed high anti-precipitation performance and good stability for 100 h of measurement. We believe that this work highlights a potential strategy to solve HER electrode precipitation in seawater *via* an ingenious electrode structure design.

Data availability

Data will be made available on request.

Author contributions

Q. Liu: conceptualization, methodology, investigation, writing – original draft preparation, writing – review & editing, funding acquisition. Z. Yan: methodology, funding acquisition. J. Gao: methodology. H. Fan: methodology. M. Li: methodology. E. Wang: funding acquisition, project administration.

Conflicts of interest

There are no conflicts to declare.

Acknowledgements

The authors greatly acknowledge the financial support from the National Natural Science Foundation of China (22202203), the Strategic Priority Research Program of the Chinese Academy of Sciences (XDA 22010601), and the National Natural Science Foundation of China (grant no. 22005299). The authors would also like to thank Prof. Zhenbo Wang from the School of Chemistry and Chemical Engineering, Harbin Institute of Technology for help with the writing.

References

1 X. Li, C. Deng, Y. Kong, Q. Huo, L. Mi, J. Sun, J. Cao, J. Shao, X. Chen, W. Zhou, M. Lv, X. Chai, H. Yang, Q. Hu and C. He, *Angew. Chem., Int. Ed.*, 2023, **62**, e202309732.
2 X. Li, H. Zhang, Q. Hu, W. Zhou, J. Shao, X. Jiang, C. Feng, H. Yang and C. He, *Angew. Chem., Int. Ed.*, 2023, **62**, e202300478.
3 Q. Hu, K. Gao, X. Wang, H. Zheng, J. Cao, L. Mi, Q. Huo, H. Yang, J. Liu and C. He, *Nat. Commun.*, 2022, **13**, 3958.
4 J. Tang, X. Xu, T. Tang, Y. Zhong and Z. Shao, *Small Methods*, 2022, **6**, 2201099.
5 M. S. Genc, M. Celik and I. Karasu, *Renewable Sustainable Energy Rev.*, 2012, **16**, 6631–6646.
6 M. Chatenet, B. G. Pollet, D. R. Dekel, F. Dionigi, J. Deseure, P. Millet, R. D. Braatz, M. Z. Bazant, M. Eikerling, I. Staffell, *et al.*, *Chem. Soc. Rev.*, 2022, **51**, 4583–4762.
7 G. Calado and R. Castro, *Appl. Sci.*, 2021, **11**, 5561.
8 S. Dresp, F. Dionigi, M. Klingenhof and P. Strasser, *ACS Energy Lett.*, 2019, **4**, 933–942.
9 W. M. Tong, M. Forster, F. Dionigi, S. Dresp, R. S. Erami, P. Strasser, A. J. Cowan and P. Farras, *Nat. Energy*, 2020, **5**, 367–377.
10 Y. Kuang, M. J. Kenney, Y. T. Meng, W. H. Hung, Y. J. Liu, J. E. Huang, R. Prasanna, P. S. Li, Y. P. Li, L. Wang, *et al.*, *Proc. Natl. Acad. Sci. U. S. A.*, 2019, **116**, 6624–6629.

11 S. Bolar, S. Shit, N. Chandra Murmu and T. Kuila, *Sustainable Energy Fuels*, 2021, **5**, 5915–5945.
12 S. Khatun, H. Hirani and P. Roy, *J. Mater. Chem. A*, 2021, **9**, 74–86.
13 D. W. Kirk and A. E. Ledas, *Int. J. Hydrogen Energy*, 1982, **7**, 925–932.
14 J. H. Han, *ChemSusChem*, 2022, **15**, e202200372.
15 X. Y. Lu, J. Pan, E. Lovell, T. H. Tan, Y. H. Ng and R. Amal, *Energy Environ. Sci.*, 2018, **11**, 1898–1910.
16 Z. T. Li, X. T. Xu, X. R. Sheng, P. Lin, J. Tang, L. K. Pan, Y. V. Kaneti, T. Yang and Y. Yamauchi, *ACS Nano*, 2021, **15**, 12535–12566.
17 U. G. M. Ekanayake, D. H. Seo, K. Faershteyn, A. P. O'Mullane, H. Shon, J. MacLeod, D. Golberg and K. Ostrikov, *Sustainable Mater. Technol.*, 2020, **25**, e00181.
18 J. H. Han, *Ind. Eng. Chem. Res.*, 2022, **61**, 9165–9170.
19 P. Srimuk, X. Su, J. Yoon, D. Aurbach and V. Presser, *Nat. Rev. Mater.*, 2020, **5**, 517–538.
20 E. Jwa, N. Jeong, J. Y. Nam and J. I. Han, *Water Res.*, 2022, **220**, 118681.
21 Q. F. Liu, Z. Yan, E. D. Wang, S. L. Wang and G. Q. Sun, *Int. J. Hydrogen Energy*, 2017, **42**, 23045–23053.
22 I. W. P. Chen, C. H. Hsiao, J. Y. Huang, Y. H. Peng and C. Y. Chang, *ACS Appl. Mater. Interfaces*, 2019, **11**, 14159–14165.
23 W. L. Yu, Z. Chen, Y. L. Fu, W. P. Xiao, B. Dong, Y. M. Chai, Z. X. Wu and L. Wang, *Adv. Funct. Mater.*, 2022, **33**, 2210855.
24 J. H. Han, E. Jwa, H. Lee, E. J. Kim, J. Y. Nam, K. S. Hwang, N. Jeong, J. Choi, H. Kim, Y. C. Jeung, *et al.*, *Chem. Eng. J.*, 2022, **429**, 132383.
25 Y. Li, L. Xie and T. Su, *Carbon Manage.*, 2023, **14**, 2202167.
26 F. H. Adnan, S. Pontvianne, M. N. Pons and E. Mousset, *Chem. Eng. J.*, 2022, **431**, 133413.
27 O. Oloye and A. P. O'Mullane, *ChemSusChem*, 2021, **14**, 1767–1775.
28 H. Shi, T. Wang, J. Liu, W. Chen, S. Li, J. Liang, S. Liu, X. Liu, Z. Cai, C. Wang, D. Su, Y. Huang, L. Elbaz and Q. Li, *Nat. Commun.*, 2023, **14**, 3934.
29 T. F. O'Brien, T. V. Bommaraju and F. Hine, *Handbook of Chlor-Alkali Technology*, Springer, 2005.
30 J. Guo, Y. Zheng, Z. Hu, C. Zheng, J. Mao, K. Du, M. Jaroniec, S. Z. Qiao and T. Ling, *Nat. Energy*, 2023, **8**, 264–272.
31 M. Mohammad and M. Kaukhab, *J. Chem. Soc. Pak.*, 2011, **33**, 166–170.
32 I. Katsounaros, J. C. Meier, S. O. Klemm, A. A. Topalov, P. U. Biedermann, M. Auinger and K. J. J. Mayrhofer, *Electrochem. Commun.*, 2011, **13**, 634–637.
33 M. Auinger, I. Katsounaros, J. C. Meier, S. O. Klemm, P. U. Biedermann, A. A. Topalov, M. Rohwerder and K. J. Mayrhofer, *Phys. Chem. Chem. Phys.*, 2011, **13**, 16384–16394.
34 N. Danilovic, R. Subbaraman, D. Strmcnik, K. C. Chang, A. P. Paulikas, V. R. Stamenkovic and N. M. Markovic, *Angew. Chem., Int. Ed.*, 2012, **51**, 12495–12498.
35 X. W. Yu, J. Zhao, L. R. Zheng, Y. Tong, M. Zhang, G. C. Xu, C. Li, J. Ma and G. Q. Shi, *ACS Energy Lett.*, 2018, **3**, 237–244.
36 H. Ang and L. Hong, *J. Mater. Chem. A*, 2017, **5**, 20598–20602.
37 Q. Yang, Y. Su, C. Chi, C. T. Cherian, K. Huang, V. G. Kravets, F. C. Wang, J. C. Zhang, A. Pratt, A. N. Grigorenko, *et al.*, *Nat. Mater.*, 2017, **16**, 1198–1202.
38 J. Abraham, K. S. Vasu, C. D. Williams, K. Gopinadhan, Y. Su, C. T. Cherian, J. Dix, E. Prestat, S. J. Haigh, I. V. Grigorieva, *et al.*, *Nat. Nanotechnol.*, 2017, **12**, 546–550.
39 D. S. Hall, D. J. Lockwood, C. Bock and B. R. MacDougall, *Proc. R. Soc. A*, 2015, **471**, 20140792.
40 Y. Qu, Q. G. Zhang, F. Soyekwo, R. S. Gao, R. X. Lv, C. X. Lin, M. M. Chen, A. M. Zhu and Q. L. Liu, *Nanoscale*, 2016, **8**, 18428–18435.
41 J. Hu, X. Tang, Q. Dai, Z. Liu, H. Zhang, A. Zheng, Z. Yuan and X. Li, *Nat. Commun.*, 2021, **12**, 3409.
42 L. Shi, Z. Ying, A. Xu and Y. Cheng, *J. Phys. Chem. C*, 2021, **125**, 1240–1248.
43 P. Sun, R. Ma, X. Bai, K. Wang, H. Zhu and T. Sasaki, *Sci. Adv.*, 2017, **3**, e1602629.
44 L. Wang, M. S. H. Boutilier, P. R. Kidambi, D. Jang, N. G. Hadjiconstantinou and R. Karnik, *Nat. Nanotechnol.*, 2017, **12**, 509–522.
45 W. M. Haynes, D. R. Lide and T. J. Bruno, *CRC Handbook of Chemistry and Physics*, CRC Press, 95th edn, 2014, pp. 1–2666.